ISSN 214-453-2

CHARACTERIZATION OF HEMATITE NANOPARTICLES SYNTHESIZED VIA SOL GEL METHOD IN TWEEN 20 SURFACTANT SOLUTION

IBRAHIM ABDULKADIR[a,b] AND S. BICE MARTINCIGH[b]*

[a] Department of chemisry, Ahmadu Bello University, Sokoto expressway Samaru, Zaria, Nigeria.

[b] School of Chemistry and Physics, University of KwaZulu-Natal, Westville Campus, Private Bag X54001, Durban 4000, South Africa

[martinci@ukzn.ac.za]

ABSTRACT

Samples of hematite (α-Fe_2O_3) nanoparticles (HTW) have been synthesized through a modified sol-gel method in Tween 20 (a polysorbate surfactant), separate portions of the powders were annealed at three different temperatures (400, 500 and 600 °C). The samples were characterized by X-ray diffraction (XRD), high-resolution electron microscopy (HRTEM), Mössbauer spectroscopy and by means of a vibrating sample magnetometer (VSM). In addition, all the characterization techniques used showed the formation of phases of hematite nanoparticles with improved purity and crystallinity after higher temperature annealing. The nanoparticle size range was between 16 and 27 nm indicating good size control for Tween 20. The BET specific surface area ranged between 17 and 37 $m^2 g^{-1}$ which is also good for synthesis via solution route. The saturation magnetization and and mössbauer analysis both support the presence in the sample at lower annealing temperature of the presence of impurities of maghemite (γ-Fe_2O_3). Of particular note was the ability of Tween 20 to control the growth of the particles so that grain sizes well below 15 nm were obtained. Thus, Tween 20, when used as a surfactant in the sol-gel route, can serve to improve the physical properties of synthesized hematite nanoparticles.

Keywords*: hematite; nanoparticles; Mössbauer spectroscopy; magnetic properties; Tween 20;*

Introduction

Hematite, α-Fe_2O_3, is the most thermodynamically stable of all the known iron oxides. It exhibits n-type semiconducting properties at ambient conditions and has a band gap energy of 2.1 eV which falls within the visible region of the electromagnetic spectrum. When the oxide is prepared in nano-dimensions it exhibits novel physical and chemical properties. Lately, α-Fe_2O_3 nanoparticles have received increased interest due to some of their fascinating properties which stand out from those of the bulk material. Their low cost and non-toxicity, coupled with their wide range of applications, for example, they have found use in pigments [1, 2], lithium ion batteries and gas sensors [3, 4], catalysis [5, 6], optical and biomedical devices [7, 8], water purification [9], solar energy conversion and magnetic materials [3, 10], have made α-Fe_2O_3 nanoparticles the most investigated of all the oxides.

Nanoparticles of different shapes and sizes can form and these include nanorods [11-13], nanofibres [14, 15], nanowires [16, 17] and nanocubes [18] among others. Various techniques have been used to synthesize α-Fe_2O_3. These include hydrothermal approaches, sol-gel processes, combustion, microemulsion techniques, pyrolysis and ultrasonic-assisted methods. The sol-gel and co-precipitation methods stand out as methods capable of producing high yields of α-Fe_2O_3 nanoparticles, with sol-gel being more hands-on in terms of morphology control [19]. It is known that the synthesis conditions strongly affect the physicochemical properties of the product. Consequently, it is expected that by using a different reaction medium or adding a surfactant in the preparation process might influence some of the physical properties (e.g. size, porosity, surface area [20, 21]) of the nanoparticles.

In this paper, we report the synthesis of hematite nanoparticle via a sol-gel method in Tween 20 surfactant. powders were annealed at three different temperatures namely; 400, 500 and 600 °C and the structure, Morphology and magnetic properties determined.

Experimental

Materials: All reagents were used as received. These were $Fe(NO_3).9H_2O$ (98% Saarchem), Tween 20 (Prosynth grade Riedel-de Haën). The deionized water used was from a Millipore Milli-Q apparatus.

Methodology: Tween 20 (200 cm^3) was made up to 800 cm^3 with deionized water, $Fe(NO_3).9H_2O$ (0.03 mol) was also dissolved in deionized water (200 cm^3) and subsequently added to the Tween 20 solution dropwise with vigorous stirring. The clear yellow solution was then heated (with stirring) at 90 °C on a hot plate to form a black gel. The gel was dried in an oven at 100 °C for 24 hours and subsequently annealed in a furnace at 400 °C for 2 hours. Two separate portions were also annealed at 500 and 600 °C for 2 hours each. Hematite prepared by this method will be referred to as HTW followed by a number indicating the annealing temperature, that is, HTW400, HTW500 or HTW600.

Characterization: High and low magnification images were collected with a JEOL-JEM 2100 LAB6 high resolution transmission electron microscope (HRTEM) with a lanthanum hexaborite emission source and

operated at an acceleration voltage of 200 V and a transmission electron microscope (JEOL JEM-1010, Tokyo Japan). Each sample was dispersed in ethanol in a small centrifuge tube and sonicated before being dispersed on a carbon grid and the images collected. The crystal structures of the synthesized products were determined by powder X-ray diffraction (PXRD) on a Bruker D8 Advance instrument with a Cu K_α radiation source (λ = 1.5406 Å). Diffractograms were recorded between a 2θ range of 15 and 90° and the results were analyzed on the DIFFRACT ^{plus} basic evaluation package (2007). The Scherrer equation, $G = k\lambda/\beta\cos\theta$ (where K is the Scherrer constant of 0.89, λ is the wavelength of radiation and β is the full width at half maximum) was used to calculate the grain sizes of the particles. Surface area analysis was performed on a Micromeritics Tristar II 3020 fully automated three-station surface area and porosity analyzer using nitrogen at 77 K. The magnetic properties were determined with a LakeShore 735 vibrating sample magnetometer (VSM) which had been calibrated by a standard Ni sphere of saturation magnetization 54.7 emu g^{-1}. The magnetization curve was obtain at a maximum magnetic field of 14 kOe at room temperature. The zero-field ^{57}Fe Mössbauer spectra were obtained in transmission mode by a conventional spectrometer using a 25 mCi ^{57}Co source sealed in a rhodium matrix and vibrated at constant acceleration. The spectrometer was calibrated with a natural α-iron foil and all measurements were made at room temperature. The spectra were then fitted with the aid of Recoil Mössbauer fitting software.

Phase Purity and Crystallinity: The powders all formed with a reddish brown colour. HTW400 was darker and finer while 500 and 600 appeared lighter in colour. The X-ray diffraction patterns for the three samples are shown in Figure 1. The XRD patterns are similar and all display peaks typical of hematite which is in agreement with reported α-Fe_2O_3 peak positions (JCPDS No. 33-0664) [22]. Smaller peaks which occur at 2θ values between 29.3295 and 33.159° are due to impurities and can be seen on the diffractogram of HTW400. Likely impurities that could be generated alongside α-Fe_2O_3 are Fe_3O_4, γ-Fe_2O_3 and oxyhydrites (i.e. α-, γ-, or amorphous FeOOH) [23-25]. The peak at the 2θ value of 29.3295° corresponds to the position of the (220) peak for Fe_3O_4 and γ-Fe_2O_3 which are both spinels. Also the (110) α-Fe_2O_3 peak intensities for HTW400 are abnormally high relative to their corresponding (104) peaks. This could be attributed to the fact that the (110) α-Fe_2O_3 peak position corresponds to the spinel (311) peak position for Fe_3O_4 and γ-Fe_2O_3 [26, 27]. This larger than expected intensity may be due to contributions from both sources thus confirming the presence of either α-Fe_2O_3 or γ-Fe_2O_3 phases in HTW400 sample [23]. The peak intensity is generally low; this indicates poor crystallization for the powder annealed at 400 °C. XRD peaks for powders annealed at higher temperatures (500 and 600 °C), however, show a significant increase in peak intensity and an adjustment of the peaks to normal α-Fe_2O_3 peak ratios. Thus, the purity and crystallinity improves with an increase in annealing temperature. The spinel (220) peak, however, is still slightly visible for HTW500, but eventually disappears for HTW600. This is an indication that the spinel impurity responsible for this peak might be γ-Fe_2O_3, and not Fe_3O_4, since γ-Fe_2O_3 is known to convert to α-Fe_2O_3 at temperatures greater than 400 °C.

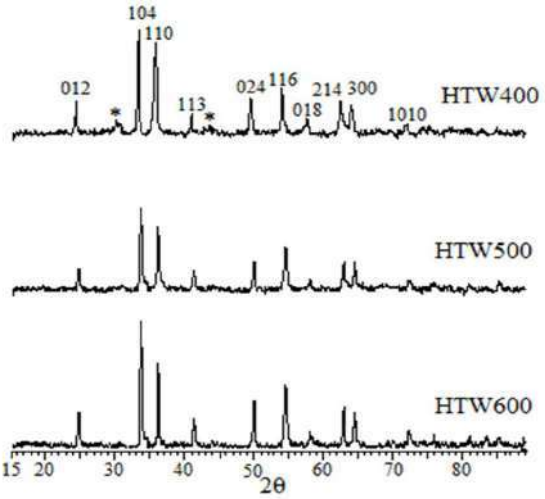

Figure 1: Powder X-ray diffractograms for hematite samples prepared by a sol gel route in Tween 20 and annealed at 400, 500 and 600 °C.

Morphology: TEM images shown in Figure 2 (a-c) confirm the crystal formation as observed from the PXRD peaks. The TEM images show nanoparticles with size ranges between 13-27 nm in agreement with calculated average size ranges from the Scherrer equation. HTW400 contains spherical nanoparticles with crystallite sizes around 13 nm, indicating that Tween 20 can effectively control the growth of crystals and limit it to between 10 and 15 nm. The crystallite sizes increased to around 18-20 nm for HTW500 and to around 25nm for HTW600 showing a gradual increase in crystallite sizes with increasing annealing temperature. Powder crystallinity also increases with increasing annealing temperature. The HRTEM images (Figure 2c) exhibit lattice fringes for powders annealed at 600 °C showing clear d-spacing for the samples. This also explains the increase in peak intensities which were observed in the PXRD result.

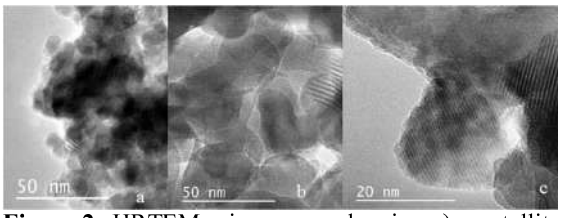

Figure 2: HRTEM micrograms showing a) crystallites HTW400 b) crystallite size increase for HTW500 and c) lattice fringed for HTW600

Surface area and porosity: The surface areas and porosities of the hematite samples were determined from nitrogen adsorption/desorption isotherms at liquid nitrogen temperature (77 K). The specific surface area was calculated with the BET model and the pore size

distribution by the BJH method. The N_2 adsorption/desorption isotherms at 77 K for the powder synthesized at 400 °C is shown in Figure 4. They conform to the type IV isotherm according to the IUPAC classification [28]. A specific surface areas (SSA) of 37.1492 $m^2 g^{-1}$was obtained which is good for powders synthesized at this temperature, indicating that Tween 20 surfactant can help improve the powder surface area because this value is larger than those reported in most cases for sol-gel and some other solution-based syntheses and for commercial hematite[29]. The hysteresis loops seen in the isotherms indicate that the powder contains porous particles with pore sizes ranging from meso- to macroporous. The BJH average pore size for HTW400 is 38.91 nm.

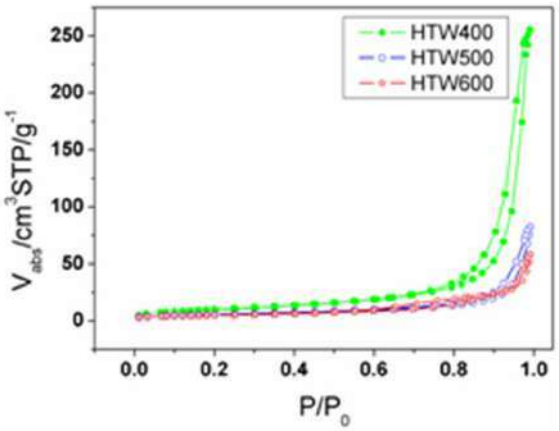

Figure 3: Adsorption-desorption isotherms in nitrogen at 77 K for HTW400, HTW500 and HTW600.

Table 1: Grain size and surface area for powders calcined at 400, 500 and 600 °C

Sample name	Grain size [nm]	Surface area [$m^2 g^{-1}$] ± 0.15
HTW400	16	37.15
HTW500	20	20.27
HTW600	26	17.15

Magnetic properties: Figure 5 shows the room temperature magnetization of the powders measured in a magnetic field of 14 kOe. The magnetization range is from 1.60 to 19.99 emu/g^{-1}. HTW400 shows an unusually high magnetization value than is normally reported for pure hematite (normally below 1 emu g^{-1}) [30-32], which is normally due to the spin canting in α-Fe_2O_3 above its Morin temperature (T_M), creating weak ferromagnetism (WF) in the sublattice [33, 34]. HTW400 shows superparamagnetic properties with a very low coercive field value (H_C) of 10 Oe. The H_C values however, increased to a value of about 301 Oe, as the annealing temperature and the crystal size G increase (see Table 2). coercivity values could be useful in describing the magnetic hardness/softness of magnetic materials; an increase in the values of these parameters would imply a tendency towards hardness and higher ferromagnetic properties [30]. The increase in H_C for HTW400 with increase in grain size and with calcination temperature indicate an increase in hardness and ferromagnetic character. However, the M_R/M_S values also increase with annealing temperature supporting this observation. The high saturation magnetization (M_S) value for HTW400 is a confirmation of the PXRD results which show the presence of small amounts of γ-Fe_2O_3 in the sample; small amounts of γ-Fe_2O_3 in α-Fe_2O_3 powder can drastically increase the M_S values [35, 36]. The decrease in the value of M_S with increasing annealing temperature however, is due to the conversion of γ-Fe_2O_3 to α-Fe_2O_3 at temperatures between 400 °C and 600 °C [22, 37].

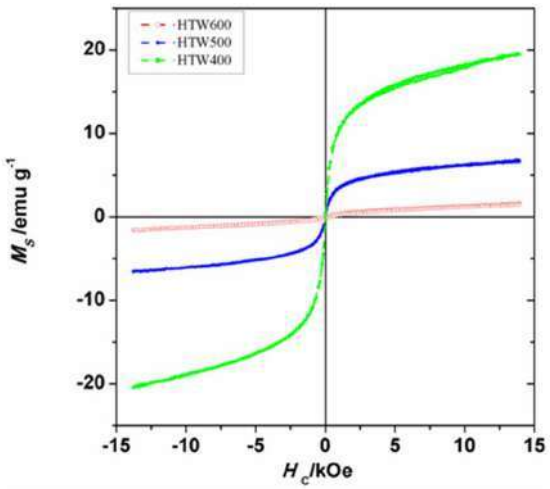

Figure 5: room temperature M-H hysteresis loops showing gradual decrease in M_S value from HTW400 to HTW600

Table 2: room temperature magnetization data for hematite powders annealed at 400, 500 and 600 °C.

Sample	G	H_C (kOe)	M_S (emu/g)	M_R (emu/g)	M_R/M_S (-)
HTW400	16	10.03	19.99	0.47	0.014
HTW500	20	20.06	6.84	0.26	0.023
HTW600	26	301.01	1.60	0.14	0.096

Mössbauer analysis: The fitted mössbauer spectrum for HTW400 is shown in Figure 6. The results of the spectral fittings are shown in Table 3. The Mössbauer parameters obtained for HTW400 indicate that the sample contains hematite and certain Fe^{3+} impurities. This impurity, as observed from the PXRD results, may either be Fe_3O_4 or γ-Fe_2O_3. Fe_3O_4 and γ-Fe_2O_3 have two distinct crystallographic sites designated A and B; The distribution of cations in spinel Fe_3O_4 and γ-Fe_2O_3 can be represented as follows $Fe^{3+}[Fe^{2+}\ Fe^{3+}]O_4$ and $Fe^{3+}[\square\ Fe^{3+}]O_3$ respectively, where □ represents a vacant octahedral (B-) site. The ions outside the parentheses are on the A- or tetrahedral site while those within the parentheses are on the B- or octahedral site. This implies that Mössbauer spectra for pure Fe_3O_4 can be fitted with two sextet subspectra with the octahedral site having twice the area of the tetrahedral site and thus its presence is easy to detect if it occurs as an impurity in α-Fe_2O_3. γ-Fe_2O_3 On the other hand, is difficult to detect in a mixture with α-Fe_2O_3 because both sites are equivalent and therefore are not distinguishable from α-Fe_2O_3. Although some reports have shown that the

isomer shift (δ) and magnetic hyperfine field (B_{hf}) for γ-Fe_2O_3 are lower than those for α-Fe_2O_3, the line between the two is very blurred and complementary PXRD data is required to make a more accurate decision [24, 38-40].

The presence of Fe_3O_4 was excluded in all samples because the B_{hf} values displayed by all the subspectra are much higher than the B_{hf} value for Fe_3O_4 (below 400 kOe). Moreover, the colour of the sample, which is reddish, does seem to suggest the absence of Fe_3O_4 which is black in colour. Samples with two or more hematite subspectra are as a result of variation in the grain sizes of the nanoparticles with larger particles having a larger B_{hf} value [41, 42]. This is expected and it agrees with the results obtained from TEM which shows that the powders contain various size ranges of nanoparticles.

The Mössbauer data collected for all the samples in this work show that the samples contain a mixture of poorly crystalline α- and γ-Fe_2O_3 at lower annealing temperatures with the well crystalline α-Fe_2O_3 phase being favored at higher annealing temperatures (see table 3). The implication of this is that both α- and γ-oxyhydroxides (FeOOH) may have been produced at the point of nucleation in the synthesis of these powders. These then converts to the corresponding Fe_2O_3 when it is annealed at 400 °C and ultimately, on increasing the annealing temperature, changes into pure α-Fe_2O_3 which is the most stable iron oxide polymorph. These could be represented according to the following reactions.

$$Fe^{3+} + 3OH^- \rightarrow (\alpha + \gamma)\text{-FeOOH} + H_2O \qquad (1)\ \text{(Nucleation)}$$

$$2(\alpha + \gamma)\text{-FeOOH} \rightarrow (\alpha + \gamma)\text{-}Fe_2O_3 + H_2O \xrightarrow{\text{heat } (>400\ ^\circ C)} \alpha\text{-}Fe_2O_3 \qquad (2)\ \text{(conversion and growth)}$$

Another scenario would be the formation of γ-FeOOH or γ-Fe_2O_3 exclusively at the point of nucleation which then converts to the corresponding γ-Fe_2O_3 at temperatures above 300 °C. γ-Fe_2O_3 is known to begin to convert to α-Fe_2O_3 at about 400 °C. The PXRD, VSM and Mössbauer spectroscopy results are all in agreement in this regard.

Conclusion

Physical and magnetic properties of α-Fe_2O_3 nanoparticles depend on the method as well as the medium in which the nanoparticles are synthesized. The synthetic routes studied in this work produced a mixture of γ- and α-Fe_2O_3 nanoparticles at an annealing temperature of 400 °C. Formation of pure crystalline α-Fe_2O_3 was favoured with increasing annealing temperature (500 and 600 °C). This was also accompanied by an increase in particle size. The PXRD, VSM and Mössbauer results are all concordant on the composition of the samples at each annealing temperature. α-Fe_2O_3 nanoparticles synthesized in Tween 20 have very small crystallite size and high BET specific surface area and improved saturation magnetization. This implies that the synthetic medium (Tween 20, a polysorbate surfactant), can be a very good additive to the precursor solution in a Pechini type sol-gel synthesis of α-Fe_2O_3 in order to effectively impact on the properties of the synthesized powders.

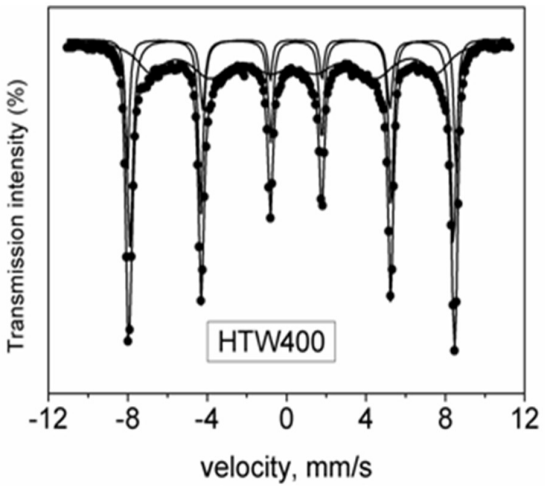

Figure 6: Mössbauer spectra for hematite samples annealed at 400 °C.

Table 3: The Mössbauer hyperfine parameters for the hematite samples prepared by different synthetic methods and annealed at 400, 500 and 600 °C. *H – hematite, MH – maghemite, (δ – isomer shift, (Δ_{EQ} – quadrupole shift, (B_{hf}) – hyperfine magnetic field and (f) – fraction population of Fe^{3+} ions at H and MH sites.

Sample	**Sublattice***	**Δ (mm/s)**	**Δ_{EQ} (mm/s)**	**B_{hf} (kOe)**	***f*** **(%)**
HTW400	H	0.36	-0.108	513.28	23.00
	H	0.37	-0.113	505.50	32.20
	MH	0.34	0.029	448.30	44.80
HTW500	*MH*	0.35	-0.002	454.60	17.10
	H	0.36	-0.11	503.52	60.00
	H	0.36	-0.10	511.87	23.00
HTW600	*H*	*0.36*	-0.21	514.16	52.00
	H	*0.37*	0.001	515.40	48.00

Acknowledgements
Ibrahim Abdulkadir is grateful to the authorities of the Ahmadu Bello University for financial assistance towards completion of this work.

References

1. Walter, D., *Characterization of synthetic hydrous hematite pigments.* Thermochimica Acta, 2006. **445**(2): p. 195-199.
2. Prim, S.R., et al., *Synthesis and characterization of hematite pigment obtained from a steel waste industry.* Journal of Hazardous Materials, 2011. **192**(3): p. 1307-1313.
3. Wu, C., et al., *Synthesis of Hematite (α-Fe_2O_3) Nanorods: Diameter-Size and Shape Effects on Their Applications in Magnetism, Lithium Ion Battery, and Gas Sensors.* The Journal of Physical Chemistry B, 2006. **110**(36): p. 17806-17812.
4. Gou, X., et al., *Monodisperse hematite porous nanospheres: synthesis, characterization, and applications for gas sensors.* Nanotechnology, 2008. **19**(12): p. 125606.
5. Tilley, S.D., et al., *Light-Induced Water Splitting with Hematite: Improved Nanostructure and Iridium Oxide Catalysis.* Angewandte Chemie, 2010. **122**(36): p. 6549-6552.
6. Herrera, F., et al., *Catalytic combustion of Orange II on hematite: Surface species responsible for the dye degradation.* Applied Catalysis B: Environmental, 2001. **29**(2): p. 147-162.
7. Xu, Y., et al., *α-Fe_2O_3 nanostructures with different morphologies: Additive-free synthesis, magnetic properties, and visible light photocatalytic properties.* Materials Letters, 2013. **92**(0): p. 321-324.
8. Tartaj, P., et al., *The Iron Oxides Strike Back: From Biomedical Applications to Energy Storage Devices and Photoelectrochemical Water Splitting.* Advanced Materials, 2011. **23**(44): p. 5243-5249.
9. Zeng, S., et al., *Hematite Hollow Spindles and Microspheres: Selective Synthesis, Growth Mechanisms, and Application in Lithium Ion Battery and Water Treatment.* The Journal of Physical Chemistry C, 2007. **111**(28): p. 10217-10225.
10. Thomann, I., et al., *Plasmon Enhanced Solar-to-Fuel Energy Conversion.* Nano Letters, 2011. **11**(8): p. 3440-3446.
11. Ramesh, R., et al., *Synthesis and properties of α-Fe_2O_3 nanorods.* Crystal Research and Technology, 2010. **45**(9): p. 965-968.
12. Gou, X., et al., *Flutelike Porous Hematite Nanorods and Branched Nanostructures: Synthesis, Characterisation and Application for Gas-Sensing.* Chemistry – A European Journal, 2008. **14**(19): p. 5996-6002.
13. Almeida, T.P., et al., *Process Map for the Hydrothermal Synthesis of α-Fe_2O_3 Nanorods.* The Journal of Physical Chemistry C, 2009. **113**(43): p. 18689-18698.
14. Zhu, Y., et al., *Preparation of superhydrophilic α-Fe_2O_3 nanofibers with tunable magnetic properties.* Thin Solid Films, 2006. **510**(1–2): p. 271-274.
15. Zheng, W., et al., *Electrospinning route for α-Fe_2O_3 ceramic nanofibers and their gas sensing properties.* Materials Research Bulletin, 2009. **44**(6): p. 1432-1436.
16. Wen, X., et al., *Controlled Growth of Large-Area, Uniform, Vertically Aligned Arrays of α-Fe_2O_3 Nanobelts and Nanowires.* The Journal of Physical Chemistry B, 2004. **109**(1): p. 215-220.
17. Wang, R., et al., *Bicrystalline Hematite Nanowires.* The Journal of Physical Chemistry B, 2005. **109**(25): p. 12245-12249.
18. Wang, S.-B., Y.-L. Min, and S.-H. Yu, *Synthesis and Magnetic Properties of Uniform Hematite Nanocubes.* The Journal of Physical Chemistry C, 2007. **111**(9): p. 3551-3554.
19. Lu, A.-H., E.L. Salabas, and F. Schüth, *Magnetic Nanoparticles: Synthesis, Protection, Functionalization, and Application.* Angewandte Chemie International Edition, 2007. **46**(8): p. 1222-1244.
20. Liu, L., et al., *Surfactant-Assisted Synthesis of α-Fe_2O_3 Nanotubes and Nanorods with Shape-Dependent Magnetic Properties.* The Journal of Physical Chemistry B, 2006. **110**(31): p. 15218-15223.
21. Housaindokht, M.R. and A. Nakhaei Pour, *Study the effect of HLB of surfactant on particle size distribution of hematite nanoparticles prepared via the reverse microemulsion.* Solid State Sciences, 2012. **14**(5): p. 622-625.
22. Darezereshki, E., *One-step synthesis of hematite (α-Fe_2O_3) nano-particles by direct thermal-decomposition of maghemite.* Materials Letters, 2011. **65**(4): p. 642-645.
23. Deraz, N.M. and A. Alarifi, *Novel processing and magnetic properties of hematite/maghemite nano-particles.* Ceramics International, 2012. **38**(5): p. 4049-4055.
24. Jacob, J. and M. Abdul Khadar, *VSM and Mössbauer study of nanostructured hematite.* Journal of Magnetism and Magnetic Materials, 2010. **322**(6): p. 614-621.
25. Žic, M., M. Ristić, and S. Musić, *57Fe Mössbauer, FT-IR and FE SEM investigation of the formation of hematite and goethite at high pH values.* Journal of Molecular Structure, 2007. **834–836**(0): p. 141-149.
26. Gaviría, J.P., et al., *Hematite to magnetite reduction monitored by Mössbauer spectroscopy and X-ray diffraction.* Physica B: Condensed Matter, 2007. **389**(1): p. 198-201.
27. Goulart, A.T., et al., *Multiple Iron-Rich Spinel Phases and Hematite in a Magnetic Soil Developing on Tuffite.* Physics and Chemistry of Minerals, 1997. **25**(1): p. 63-69.
28. Kruk, M. and M. Jaroniec, *Gas Adsorption Characterization of Ordered Organic−Inorganic Nanocomposite Materials.*

Chemistry of Materials, 2001. **13**(10): p. 3169-3183.

29. Akbar, S., et al., *Synthesis of Fe_2O_3 nanoparticles by new Sol-Gel method and their structural and magnetic characterization.*
30. Raming, T.P., et al., *The Synthesis and Magnetic Properties of Nanosized Hematite (α-Fe_2O_3) Particles.* Journal of Colloid and Interface Science, 2002. **249**(2): p. 346-350.
31. Liu, Q., et al., *The magnetism of micro-sized hematite explained.* Physics of the Earth and Planetary Interiors, 2010. **183**(3): p. 387-397.
32. Lian, J., et al., *Hematite (α-Fe_2O_3) with Various Morphologies: Ionic Liquid-Assisted Synthesis, Formation Mechanism, and Properties.* ACS Nano, 2009. **3**(11): p. 3749-3761.
33. Özdemir, Ö. and D.J. Dunlop, *Hysteresis and Coercivity of Hematite.* Journal of Geophysical Research: Solid Earth, 2014.
34. Özdemir, Ö. and D.J. Dunlop, *Thermoremanent magnetization of multidomain hematite.* Journal of Geophysical Research: Solid Earth, 2005. **110**(B9): p. B09104-B09111.
35. Ramesh, R., et al., *Synthesis and vibrational properties of hematite (α-Fe_2O_3) nanoparticles.* Journal of Materials Science: Materials in Electronics, 2011. **22**(9): p. 1357-1360.
36. Gnanaprakash, G., et al., *Magnetic nanoparticles with enhanced γ-Fe_2O_3 to α-Fe_2O_3 phase transition temperature.* Nanotechnology, 2006. **17**(23): p. 5851.
37. El Mendili, Y., et al., *Insights into the Mechanism Related to the Phase Transition from γ-Fe_2O_3 to α-Fe_2O_3 Nanoparticles Induced by Thermal Treatment and Laser Irradiation.* The Journal of Physical Chemistry C, 2012. **116**(44): p. 23785-23792.
38. Harshada, N., et al., *Mössbauer spectroscopic investigations of nanophase iron oxides synthesized by thermal plasma route.* Materials Characterization, 2008. **59**(9): p. 1215-1220.
39. Schmidbauer, E. and M. Keller, *Magnetic hysteresis properties, Mössbauer spectra and structural data of spherical 250nm particles of solid solutions.* Journal of Magnetism and Magnetic Materials, 2006. **297**(2): p. 107-117.
40. Zboril, R., M. Mashlan, and D. Petridis, *Iron(III) Oxides from Thermal ProcessesSynthesis, Structural and Magnetic Properties, Mössbauer Spectroscopy Characterization, and Applications†.* Chemistry of Materials, 2002. **14**(3): p. 969-982.
41. Lemine, O.M., et al., *Rietveld analysis and Mössbauer spectroscopy studies of nanocrystalline hematite α-Fe_2O_3.* Journal of Alloys and Compounds, 2010. **502**(2): p. 279-282.
42. Gangs, N.H., et al., *Mössbauer Studies of Small Particles of Iron Oxides in Soil.* Clays and Clay Minerals, 1973. **21**(3): p. 151-160.